Chemical Engineering Journal 505 (2025) 159558

Contents lists available at ScienceDirect

Chemical Engineering Journal

journal homepage: www.elsevier.com/locate/cej

Self-Sensing shape memory boron Phenolic-Formaldehyde aerogels with tunable heat insulation for smart thermal protection systems

Likai Hu [a], Lan Luo [a], Fenghua Zhang [a,*], Yanju Liu [b], Jinsong Leng [a,*]

[a] Centre for Composite Materials and Structures, Harbin Institute of Technology (HIT), Harbin 150080, PR China
[b] Department of Astronautical Science and Mechanics, Harbin Institute of Technology (HIT), Harbin 150001, PR China

ARTICLE INFO

Keywords:
Shape memory polymers
Phenolic resin
Ablation property
Aerogel
Thermal protection

ABSTRACT

With the rapid development of new-generation aviation and space vehicles, the demand for deformable thermal protection systems and material technologies has emerged. Phenolic aerogels are appealing insulation materials for thermal protection. However, their inherent brittleness restricts their application. It is crucial to develop phenolic resins with high-temperature resistance and aerogels with excellent tunable thermal insulation properties to ensure a reliable smart thermal protection system. Herein, shape memory boron phenolic-formaldehyde resins with hyperbranched topologies were developed, which retained a 65 % residual mass under nitrogen at 1000 ℃ and a line ablation rate of 0.048 mm/s. The resins were endowed with excellent shape memory properties by the boron-oxygen bonds introduced into the cross-linking network. Shape memory boron phenolic-formaldehyde aerogels (SMBPFAs) with low density (0.18 g/cm^3) and high porosity (89.3 %) were fabricated via template-in-situ polymerization. SMBPFAs exhibited outstanding thermal insulation performance and could withstand a 800 ℃ flame while maintaining a cold side temperature of only 162 ℃. Remarkably, SMBPFAs in temporary shapes can precisely regulate the thermal insulation performance on demand by altering the microstructure through shape recovery. As a proof-of-concept, we look forward to the application of SMBPFAs in smart thermal protection systems for future aircraft.

1. Introduction

The dynamic development of various flight vehicles has led to higher requirements for thermal protection systems, and aerogels have become an ideal choice due to their unique properties. Numerous studies have demonstrated that aerogels were among the most promising thermal protection materials within the aerospace field [1–3]. Their light weight, excellent thermal insulation and flexibility allow them to adapt to the deformation requirements of flight vehicles and provide an effective guarantee of thermal protection [4–6]. Inorganic aerogels exhibit excellent thermal insulation performance; however, their poor mechanical properties limit their widespread application [7–9]. In 1989, Pekala prepared organic aerogels for the first time using a sol–gel reaction between resorcinol and formaldehyde, pioneering the use of organic aerogels [10].

As an engineering polymer that has been around for a century, phenolic-formaldehyde resins (PFs) were first synthesized by Bayer in 1872 [11], and developed into a new high-performance engineering plastic with ultrahigh commercial value in the 20th century. PFs have excellent thermal stability and ablative properties [12–14], and are promising materials for ablative heat protection [15,16]. Over time, PFs have been associated with brittleness and a lack of elasticity [17]; however, this stereotype can be eliminated by rational molecular or product structure design. The molecular chains of PFs are rich in chemically active hydroxyl groups, and utilizing these hydroxyl groups to graft or copolymerize with other polymers has become the mainstream approach for PF toughening [18–21]. Lin-Gibson et al. [22] modified PFs with a bisphenol A-type epoxy resin acting as a cross-linking agent, which improved the toughness and processability of the PF. Li et al. [23] blended cyanoacrylate ester with PFs, which resulted in the formation of a flexible structure during curing and improved the mechanical properties of the resin. Deng et al. [24] copolymerized polyurethane prepolymers with methyl-ordered phenolics, which reduced the crosslink density of PFs, and synthesized a primordial shape memory phenolic resin, endowing PFs with deformability. These modifications tend to sacrifice some of the thermal stability properties while improving the toughness of PFs, which limits their application in high-temperature environments. Therefore, there is an urgent need to

* Corresponding authors at: Centre for Composite Materials and Structures, Harbin Institute of Technology (HIT), Harbin 150080, PR China (F. Zhang).
E-mail addresses: fhzhang_hit@163.com (F. Zhang), lengjs@hit.edu.cn (J. Leng).

https://doi.org/10.1016/j.cej.2025.159558
Received 29 October 2024; Received in revised form 21 December 2024; Accepted 12 January 2025
Available online 13 January 2025

develop PFs with both high mechanical properties and high-temperature resistance [25].

The emergence of nanotechnology has injected new vitality into PFs, leading them into the era of nanomaterials [26,27]. In recent decades, PFs have experienced a revival and secondary boom. The emergence of phenolic aerogels has broadened their applications to fire protection, thermal insulation and other fields [28–32]. Various strategies have been developed to prepare phenolic aerogels with multifunctional mechanical properties [33–35]. Yang et al. [36] realized the copolymerization of polyurethane and phenolic resins through a sol–gel strategy, and prepared polyurethane (PU) – modified phenolic aerogels with good thermal stability and thermal insulation by atmospheric pressure drying. It was found that the structure of the aerogel could be controlled by using the template method, and that the density of the aerogel could be precisely controlled by controlling the ratio of the template to the raw material [37]. The phase separation strategy can adjust the phenolic aerogel backbone morphology. Yu et al. [38] prepared PF/SiO_2 composite aerogels with three-dimensional binary networks by using copolymerization and nanoscale phase separation strategies, and this approach endowed the PF/SiO_2 aerogels with excellent mechanical resilience, thermal insulation, and flame-retardant properties. The phenolic aerogels reported thus far have obvious deficiencies in controlling the deformation process, and the synergy of thermal-insulation and shape memory properties can dynamically adjust the thermal-insulation effect according to the ambient temperature and demand, which is expected to expand the application of phenolic aerogels. The rapid development of the aerospace industry puts forward a demand for smart thermal protection systems [39], which can sense external temperature changes in real-time and adjust the protection strategy to automatically realize more accurate and efficient thermal protection. Therefore, there is an urgent to develop aerogel materials with active thermal insulation performance.

Herein, a hyperbranched topology design strategy has been proposed to synthesize shape memory boron phenolic-formaldehyde resins (SMBPFs) with high thermal stability. The large number of benzene rings in the molecular structure of SMBPFs enable excellent ablation properties, and the toughness of the boron-oxygen bonds allows the material to possess shape memory properties without loss of thermal stability. Subsequently, insulating shape-memory boron phenolic-formaldehyde aerogels (SMBPFAs) with low density and high porosity were generated on the template by an in-situ polymerization strategy using sodium chloride as a template, taking advantage of active dehydration and pore creation during the polymerization of PFs. The synergistic effect of shape memory properties and thermal insulation properties enables the SMBPFAs to accurately regulate their thermal insulation capability. In a word, our work broadens the application prospects of phenolic aerogels and promises to apply the SMBPFAs to smart thermal protection systems for future aircraft.

2. Experimental section

2.1. Synthesis of shape memory boron phenolic resins

The synthesis of SMBPFs consisted of two steps: the synthesis of 4,4′-oxybis(2-(hydroxymethyl) phenol) and the synthesis of boron phenolic resins. Firstly, 4,4-dihydroxydiphenyl ether and ethanol were added to a three-necked round-bottomed flask at 60 ℃ in an oil bath to dissolve. Secondly, formaldehyde solution and barium hydroxide pentahydrate were added to get 4,4′-oxybis(2-(hydroxymethyl) phenol) by reacting at 90 ℃ for 2 h under nitrogen environment. Thirdly, boric acid was added to the three round-bottomed flasks in batches, while the reaction temperature increased to 100 ℃. Boron phenolic resin prepolymers with different degrees of branching were obtained by controlling the reaction amount of boric acid, then barium borate precipitation generated during the reaction process was removed by purification. Finally, the boron phenolic resin prepolymer was poured into the mold and cured according to 90 ℃/2h, 100 ℃/2h, 110 ℃/2h, 120 ℃/2h, 130 ℃/10 h to finally obtain the SMBPFs. The high-quality fabrication of the material serves as the pivotal determinant in guaranteeing its outstanding performance. It is noteworthy that the hot-pressing strategy was adopted during the curing stage of SMBPFs. This ensured that any bubbles formed during the process were effectively expelled from the material, thereby facilitating the efficient production of bubble-free SMBPFs. According to the different branching degrees of the resin, the SMBPFs were labeled with SMBPF-1, SMBPF-2, SMBPF-3, SMBPF-4, SMBPF-5, SMBPF-6, and SMBPF-7, respectively.

2.2. Preparation of shape memory boron phenolic aerogels

The SMBPFAs were prepared as follows: SMBPFAs prepolymer and sodium chloride particles were mixed and broken into powder by a pulverizer to make a homogeneous mixture, which was pressed into block embryos through molds. The block embryos were cured at 130 °C for 12 h to obtain prepared SMBPFAs, which were subjected to a de-templating process to obtain SMBPFAs. According to the proportion of boron phenolic resin prepolymer, SMBPFAs were labeled with 10 wt %-SMBPFA, 15 wt%-SMBPFA, 20 wt%-SMBPFA, 25 wt%-SMBPFA, and 30 wt%-SMBPFA, respectively.

2.3. Characterization

The chemical bonding of SMBPFs was determined by a Nicolet iS10 (Nicolet Instrument Crop) infrared spectrometer analyzer with a resolution of 4 cm^{-1} in the wavelength range of 4000 to 500 cm^{-1}. The thermogravimetric profiles of samples with an initial mass of 15–20 mg were determined by thermogravimetric analysis (TGA/DSC1, Mittler Toledo) in the temperature range of 25–1000 ℃ in a flowing nitrogen atmosphere at a temperature increase rate of 10 ℃/min. The storage modulus and tan delta of samples of 30 x 3 x 1 mm were determined within the temperature range of 25–300 ℃ via a dynamic thermodynamic analyzer (DMA, NETZSCH Q800, TA). The T_g of the material was determined by differential scanning calorimetry with tests conducted in a nitrogen atmosphere heated from 25 to 300 ℃ at a rate of 10 ℃/min. The mechanical properties of SMBPFs and SMBPFAs were investigated by the Zwick/Roell Z010 universal material testing machine, in which high-temperature tensile tests were conducted in the range of 60–120 ℃. Microstructural images of SMBPFs and SMBPFAs were obtained by secondary electron mode scanning with a scanning electron microscope (Tescen), and all samples were gold-sprayed for 200 s prior to testing. The ablative properties of SMBPFs were determined using the GJB323A96 standard with an oxygen flow rate of 1512 L/h and an acetylene flow rate of 1116 L/h. The sample size was: 29.4 mm in diameter and 15 mm in thickness. The densities of the SMBPFAs were all calculated by measuring the apparent volume and density. Five different samples of each SMBPFA specimen were prepared to derive mean values and errors. The pore size distribution of SMBPFAs was determined by the BET method (ASAP 2020, Micromeritics Inc.). The dynamic mechanical properties of SMBPFAs, as well as shape memory cycling, were measured by the compression mode of the Q800 with aerogel sample sizes of 10 mm in diameter and 10 mm in thickness. The thermal conductivity of SMBPFs at 25 ℃ and 100 ℃ was measured by the HOT-DISK method. Infrared thermographic photographs of the SMBPFs were obtained by a Sony infrared camera. Temperatures of the SMBPFAs were measured with thermocouples connected to a temperature acquisition system (THA9, TENGHUI Ltd.).

The shape memory properties of SMBPFAs were characterized by the shape fixity rate and recovery rate of the materials which were calculated according to the following equations:

$$R_f = \frac{h_1 - h_3}{h_1 - h_2} \times 100\%$$

Where R_f is the fixity rate of SMBPFAs; h_1 is the initial height of

SMBPFAs; h_2 is the height of SMBPFAs after cooling and unloading; h_3 is the height of SMBPFAs after an interval.

$$R_r = \frac{h}{h_1} \times 100\%$$

Where R_r is the recovery rate of the SMBPFAs; h_1 is the initial height of the SMBPFAs; h is the height of the SMBPFAs after recovery.

3. Results and Discussion

3.1. Design strategy of SMBPFs

A novel phenolic resin with shape memory properties and resistance was designed at extremely high temperatures under the guidance of a hyperbranching mechanism. Consecutive adjacent benzene rings are key to their high thermal stability, while the topological network structure triggered by boron-oxygen bonding leads to improved mechanical properties. The hot-press method can minimize the generation of air bubbles during the dehydration process of phenolic curing. Based on these principles, boric acid was used to build topological network structures for constructing SMBPFs that combine deformation and thermostable properties. The synthesis and preparation process of SMBPFs is shown in Fig. 1a, and the specific formula was shown in Table S1. The chemical structure of 4,4′-oxybis(2-(hydroxymethyl) phenol) is determined by Fourier transform infrared spectroscopy (FTIR) and ^{1}H NMR spectroscopy, as shown in Fig. S1 and Fig. S2. The emergence of characteristic peaks associated with ph-CH_2-OH and ph-O-ph implied that the reaction was successful. The multiple peaks, densely distributed at 6.8 ppm, 6.84 ppm, 7.03 ppm, and 7.12 ppm, corresponded to the vibrational frequencies of hydrogen protons presented in both the benzene rings and alcohol hydroxyl group within the target products. Additionally, resonance peaks corresponding to the hydrogen protons on the carbon atoms of ph-CH_2-OH were observed at 4.61 ppm. The resonant frequency of the hydrogen protons associated with the phenol hydroxyl group was detected at 9.68 ppm. The curing temperatures of SMBPFs were determined by the rheological curve, as shown in Fig. S3. The chemical structures of the SMBPFs were determined by FTIR spectroscopy, and all curves were calibrated and analyzed, as shown in Fig. 1b. The FTIR analysis of the SMBPFs revealed some important characteristic peaks. The C-H peak of the neighboring substitution of the benzene rings was observed at 790 cm^{-1}; the telescopic vibrational peak associated with ph-CH_2-OH appeared at 1020 cm^{-1}; and the characteristic peak of ph-O-ph appeared at 1220 cm^{-1}. These observations implied that formaldehyde and 4,4-diphenyl ether underwent additional reactions. The stretching vibration peak of the B-O bond at 1370 cm^{-1} was also observed, providing further confirmation of the successful implementation of the branching reaction in the phenolic resin. The thermal stability of the SMBPFs was evaluated by TGA, as depicted in Fig. 1c and 1d. The introduction of boric acid led to the formation of B-O bonds possessing high bond energy throughout the reaction. The bond

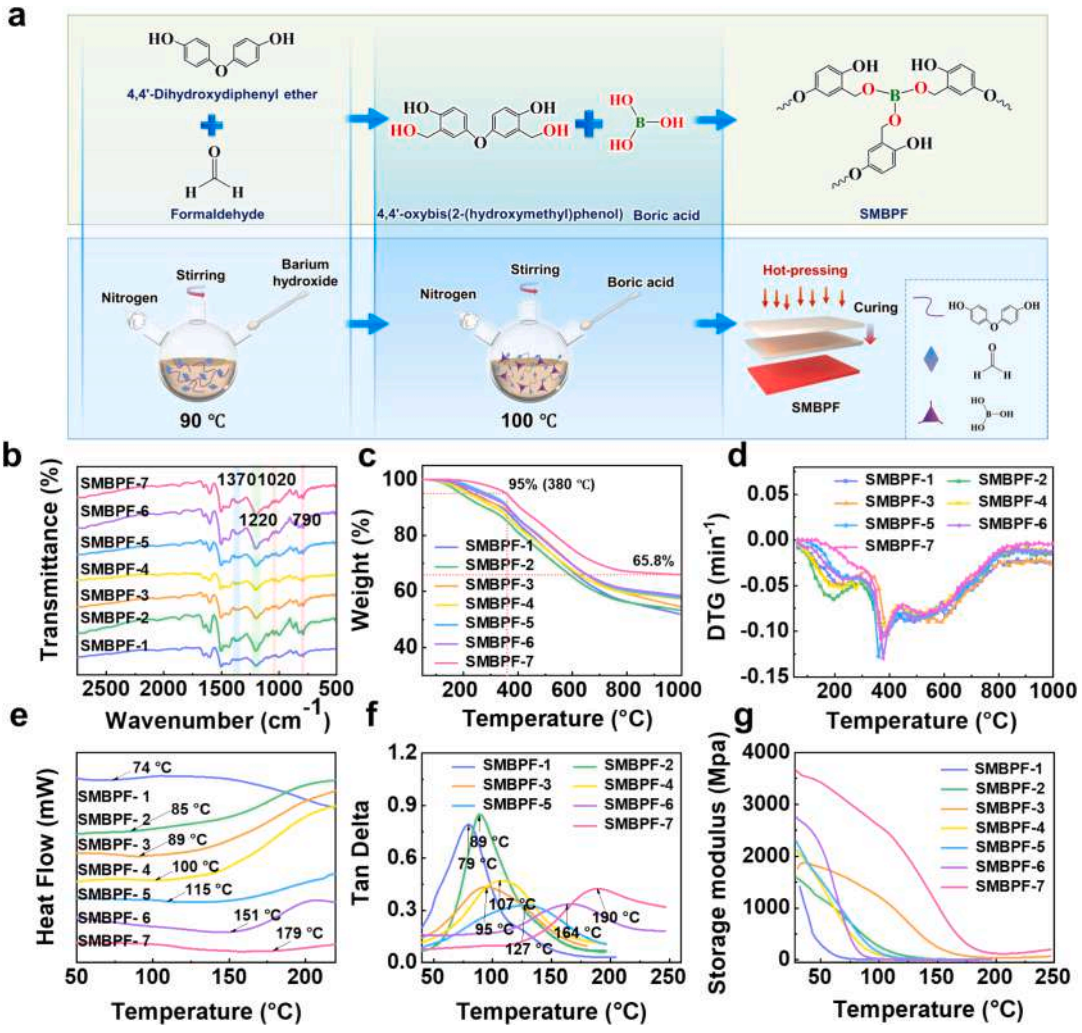

Fig. 1. Synthesis and properties of SMBPFs. a) Schematic illustration for the preparation of SMBPFs. b) The FTIR spectra of SMBPFs. c) The TGA curves of SMBPFs. d) The DTG curves of SMBPFs. e) The DSC curves of SMBPFs. f-g) The DMA curves of SMBPFs.

energy of the B-O bond is significantly higher than those of the C-C and C-O bonds in ordinary polymers, enabling it to resist thermal decomposition reactions to a certain extent. Consequently, the thermal stability of the resin was enhanced. The introduction of the B-O bonds could also remarkably augment the carbon residue rate of the material, thereby improving its thermal stability. [40] Overall, all SMBPFs exhibited mass residual rates higher than 55 % when subjected to a nitrogen environment at 1000 °C. Notably, the highly branched SMBPF-7 demonstrated the highest mass residual rate of 65.8 %, surpassing the corresponding rates of the reported shape memory phenolic resins. Additionally, it reached a temperature of only 380 °C when experiencing a mass loss of 5 %, thus exemplifying the exceptional thermal stability possessed by SMBPFs.

The thermal degradation process of the SMBPFs was analyzed using DTG curves. In the first stage (50 – 350 °C), the predominant mechanism involved the cleavage of residual small molecules in SMBPFs, resulting in a mass loss ranging from 5 % to 9 %. In the second stage (350 – 800 °C), the phenolic main chain underwent fracture, accompanied by the breaking of B-O-C bonds and generation of B-O bonds. In the transition to the third stage (800 – 1000 °C), elemental boron reacted with elemental oxygen to form a ceramic layer that encapsulated the outer surface of specimens, effectively protecting them from significant mass loss. At this stage, the SMBPFs experienced a mass reduction of approximately 3 % – 5 %. The DSC curves of the SMBPFs are shown in Fig. 1e. Specifically, as the number of branched sites and density of branches in the linear phenolic long chains increased, the glass transition temperature (T_g) of the SMBPFs gradually shifted toward higher temperatures from 74 °C to 179 °C. The temperature range for utilizing the SMBPFs is determined by their collective thermal stability and thermomechanical properties. The dynamic mechanical analysis (DMA) curve was employed to analyze the dynamic mechanical properties of the SMBPFs, as illustrated in Fig. 1f and 1 g. With an increasing degree of hyperbranching, a gradual decrease in the abundance of flexible long chains within the SMBPFs occurred, resulting in the migration of the tan delta peak towards higher temperatures. Owing to the variations in the testing principles, slight disparities were observed between the measured results and those obtained using DSC. Notably, SMBPF-1 exhibited a low glass transition temperature at 79 °C, while SMBPF-7 displayed a high T_g of 190 °C. Furthermore, an increase in the amount of boric acid involved in the reaction resulted in the gradual generation of SMBPFs with varying degrees of branching, leading to a progressive broadening of the tan delta peak. As the temperature increased, a gradual decrease in the SMBPFs was observed, effectively showcasing their variable stiffness characteristics. Additionally, the energy storage modulus of the SMBPFs decreased and reached less than 100 MPa upon reaching T_g. This indicated the successful completion of the material deformation process. The hyperbranched phenolic resin was ingeniously engineered by incorporating boric acid, thereby facilitating the synthesis of SMBPFs with exceptional thermal stability.

3.2. Mechanical and shape memory performance of SMBPFs

The mechanical properties of materials play a pivotal role in determining their applicability. However, the brittleness and inadequate mechanical properties of PF, which present challenges for their utilization in load-bearing structures, have long been widely recognized in the

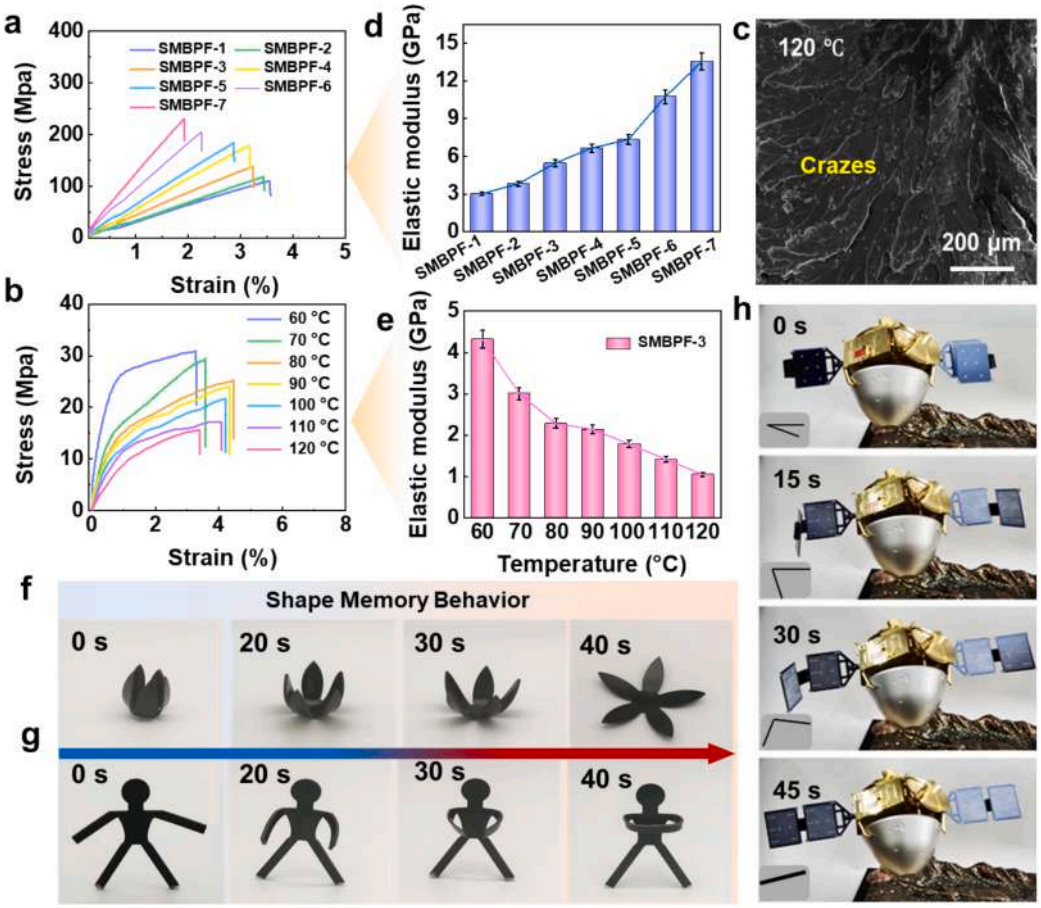

Fig. 2. Mechanical properties and shape memory properties of SMBPFs. a) The tensile stress–strain curve of SMBPFs at room temperature. b) The tensile stress–strain curve of SMBPFs at high temperature. c) The elastic modulus of SMBPFs at room temperature. d) The elastic modulus of SMBPFs at high temperature. e) The SEM images of SMBPFs tensile fracture. f-g) Shape memory recovery process of SMBPFs. h) The potential spatial applications of SMBPFs.

academic community. The mechanical properties of the SMBPFs were significantly enhanced by the boric acid hyperbranching treatment. The tensile stress–strain curves of SMBPFs at room temperature exhibited typical brittle fracture characteristics, as depicted in Fig. 2a. The curve is confined to the elastic deformation stage, with fractures occurring prior to any plastic deformation. The mechanical properties of the polymers are influenced by the network density of their molecular structures. Notably, the highly branched SMBPF-7 demonstrated exceptional tensile strength reaching 228.9 MPa, whereas samples with lower degrees of branching displayed comparatively lower tensile strengths. The hyperbranched structure imparted remarkable structural stability to the material, even in cases where branching was minimal, resulting in an elongation-at-break of 3.5 %. In addition, the elongation at the break of the other samples decreased progressively with an increasing degree of branching. To comprehensively study the high-temperature tensile properties, SMBPF-3 with a moderate degree of branching and a glass transition temperature of 95 °C was selected as an effective specimen considering its practical applicability within the temperature range. The high-temperature tensile behavior of SMBPFs was investigated in the range of 60 to 120 °C, as depicted in Fig. 2b. At elevated temperatures, ductile fracture behavior was observed for SMBPF-3, in which fractures occurred prior to reaching the yield strength, rendering it challenging to discern the yield stage on the stress–strain curve. Consequently, the material exhibited an initial elastic response followed by plastic deformation before fracturing. The scanning electron microscopy (SEM) image in Fig. 2c showcases crazes at the fracture site. The presence of crazes at the fracture site further confirmed the occurrence of ductile fractures in the material. Upon heating to 60 °C, the material reached a highly elastic state, thereby enhancing its capacity for elastic deformation. As the temperature continued to increase, the material exhibited increased pliability and elongation-at-rupture compared to that at room temperature. Notably, at 80 °C below the T_g, maximum elongation at rupture reached 4.4 %. Before this threshold, the elongation-at-rupture increased with increasing temperature; however, beyond this point, it demonstrated a declining trend.

In addition, the tensile strength decreased significantly as the temperature increased and continued to decline progressively. At 120 °C, its tensile strength was only 15.6 MPa, which is much lower than the strength at room temperature. The greater the degree of branching in a material, the denser its network, resulting in increased resistance to deformation and higher tensile modulus. As shown in Fig. 2d, SMBPF-7 exhibited the highest tensile modulus of 13.53 GPa, whereas SMBPF-1 displayed the lowest at 3.03 GPa. An increase in temperature accelerated the molecular thermal movement within the material, altering its mechanical properties as the molecular chains experienced enhanced mobility and gradually reduced the material's modulus over time. As illustrated in Fig. 2e, the tensile modulus of SMBPF-3 decreased from 4.32 GPa at 70 °C to 1.05 GPa at 130 °C.

In accordance with the previous research findings, the shape memory performance of SMBPFs was evaluated via a bending-recovery test. [41] The shape recovery rate, as well as the fixity rate of SMBPFs, were presented in Table S3. SMBPFs exhibited favorable shape memory capabilities, SMBPF-3 possessed the highest shape fixity and recovery rates, both attaining 99 %. As the degree of branching augmented, the recovery rate declined to a certain extent, with the lowest recovery rate of SMBPF-7 being 92 %. The extraordinary shape memory performance exhibited by the SMBPFs is shown in Fig. 2f, where a diminutive figurine momentarily assumes an alternate form to showcase the holding fist salute, reminiscent of the traditional Chinese Kung Fu movements. Furthermore, Fig. 2g presents an awe-inspiring demonstration of the remarkable shape memory capabilities of SMBPFs as they seamlessly transition from bud to blossom with grace and precision. The interesting shape recovery process of SMBPFs was also demonstrated in Fig. S4 and Video S1. In addition to providing elegant and enjoyable demonstrations, SMBPFs are also anticipated to have practical applications in deep space exploration projects such as missions to the Lunar and Mars. Fig. 2h and Video S2 illustrate the deployable structures of the SMBPFs integrated into the solar panels of lunar exploration vehicles, enabling swift deployment upon thermal stimulation within a condensed timeframe. This technological advancement is expected to yield substantial cost savings and enhance researchers' operational efficiency.

3.3. Ablation mechanism of SMBPFs

Rapid advancements in supersonic vehicle technology have presented unique challenges for thermal protection systems, particularly when confronted with diverse vehicle designs. It is anticipated that a smart thermal protection system can seamlessly integrate deformation and variation capabilities while upholding exceptional thermal protection. PFs, as a conventional choice for ablative materials, show remarkable attributes such as low density, outstanding oxidation resistance, and high temperature endurance. The SMBPFs developed in this study exhibit exceptional resistance to ablation. Furthermore, incorporating boron facilitates forming a protective ceramic layer on the surface of the ablated material, effectively preventing high-temperature failure. The ablation mechanism is illustrated in Fig. 3a.

The ablation process entails the extraction of substances through intense scouring and stripping, facilitated by chemical and physical interactions with scorching temperatures, immense pressure, and rapid combustion gas flow. This results in profound energy conversion and material attrition. The ablation behavior test of SMBPFs was conducted at a scorching flame temperature of 2500 °C for 30 s, as shown in Fig. S5 and Video S3. Initially, the fire blaze penetrated the central region of material and subsequently propagated towards the periphery with an increasingly dwindling flow rate. Captured through optical lenses (Fig. 3b (I and II)), post-ablation photographs were utilized to classify the intricate structure of the SMBPFs into two distinct regions, the center and edge, based on their respective distances from the epicenter of ablation. The mechanism of the oxyacetylene ablation of material can be classified into two categories: high-temperature oxidation and mechanical stripping. In the central region, where oxygen density and flow rate reached their peak levels, a vigorous oxidation reaction ensued, resulting in the formation of ablation craters with a depth of approximately 3000 μm in the center region under the erosion caused by high-speed airflow and an extreme temperature of 2500 °C (Fig. 3b (III and V)). Concurrently, holes and cracks were formed. The central region was subjected to an exceedingly high-temperature environment, which resulted in a multitude of intricate chemical reactions. The B-O bonds within the material were broken during the ablation of the material. The boron released therefrom reacted with the carbon produced by resin carbonization to form boron carbide, which possessed higher thermal stability and ablative resistance. A portion of the resulting B_4C was oxidized and metamorphosed into B_2O_3 in the presence of elevated temperatures and oxygen flow. Consequently, an ultimate ceramic layer composed of B_4C, B_2O_3, and glassy carbon materialized on the surface of the ablation center region. This ceramic layer adhered to the surface of the material, thereby enhancing the thermal protection performance of the material. The XRD curves of the SMBPF after oxyacetylene ablation can effectively determine the generated ceramics, as shown in Fig. S6. The ceramic layer served as a protective barrier for the unablated inner region, while also facilitating efficient heat dissipation through surface ablation. As evidenced by the optical image of the fractured cross-section (Fig. 3b (IV)) and the three-dimensional depth-of-field microscope image (Fig. 3b (VI)), the interior area of the sample remained predominantly intact owing to its inability to come into direct contact with the flame. The temporal variations in the surface temperatures of the ablated specimens are shown in Fig. 3c. Upon ignition of the ablation flame, the surface temperature of the sample rapidly soared to approximately 2500 °C and gradually reached a state of equilibrium. The evaluation of a material's resistance to ablation relies heavily on its mass and line ablation rates. The mass and line ablation rates of the SMBPFs were determined to be 0.080 g/s and 0.043 mm/s, respectively, based

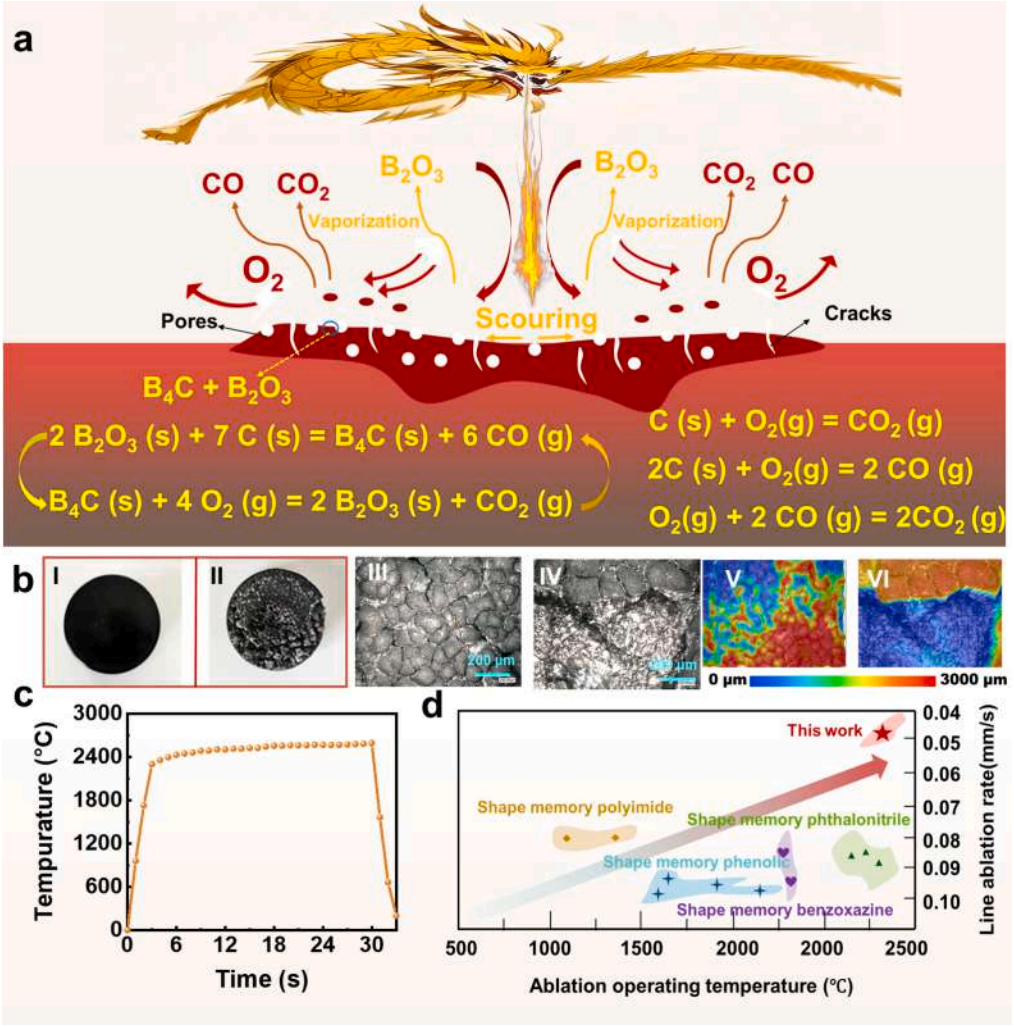

Fig. 3. Ablative performance of SMBPFs. a) The ablative mechanism of SMBPFs. b) The physical and three-dimensional depth of field pictures of SMBPFs. c) The ablative test curve of SMBPFs. d) The comparison of ablative properties of shape memory polymers[41–43].

on a 30-second test. Both of these rates are considered exceptional among the reported data for shape memory polymers, as shown in Fig. 3d. From a practical application perspective, ablation materials face the dual challenge of withstanding high temperatures while simultaneously enduring stress fields. Drop-weight impact tests were conducted to characterize the impact resistance of SMBPF and systematically evaluate their performance under such conditions. The velocity change of the hammer head and the energy absorption curve of the material during the test were illustrated in Fig. S7. The impact resistance of the material remarkably decreased the speed of the hammer head upon contacting the SMBPF sample. The test results indicated that the SMBPF had favorable impact resistance and the impact strength was 4.26 KJ/m^2. The comprehensive characterization results mentioned above demonstrated that SMBPF possessed outstanding ablation resistance performance along with favorable impact resistance property, which endowed it with broad application prospects in the field of ablative materials. In summary, the incorporation of boron and the implementation of hyperbranching not only resulted in remarkable shape memory properties of the PFs, but also significantly enhanced their ablation resistance, thereby facilitating their application in thermal protection systems.

3.4. Construction of SMBPFAs

The matrix chosen for its practical application requirements was SMBPF-3, which has a deformation temperature of 95 °C. Sodium chloride was utilized as a template for the in-situ polymerization of pre-cured boron phenolic resin powder to construct a three-dimensional network structure and fabricate SMBPFAs with a porous morphology. The preparation process of the SMBPFAs is depicted in Fig. 4a, and the specific formulas are shown in Table S2. Subsequent removal of the sodium chloride template resulted in the formation of micron-scale pores within the intricate structure of the aerogel. The observed SEM images (Fig. 4b) revealed that these exquisite micron-scale pores exhibited a size range spanning from 2 to 10 μm. During the curing process, water molecules are generated through resin polymerization, resulting in the dissolution of NaCl particles and their subsequent infiltration into the aerogel structure, which leads to the formation of nanoscale pores. Consequently, these minute nanosized pores could be clearly observed to be attached to the pore walls within the microstructure of the aerogels. The implementation of multiple pore-formation processes resulted in the creation of aerogels with exceptionally low densities and significantly elevated porosities.

Furthermore, the SMBPFs endowed the aerogels with unique shape memory properties. The microstructures of the SMBPFAs before and after shape memory assignment are shown in Fig. 4c. After 40 % compressive deformation, pronounced compression was observed within the microstructures of the SMBPFAs, which led to pore flattening. After thermal stimulation, the aerogel exhibited remarkable shape memory behavior and its microstructure underwent shape recovery. The

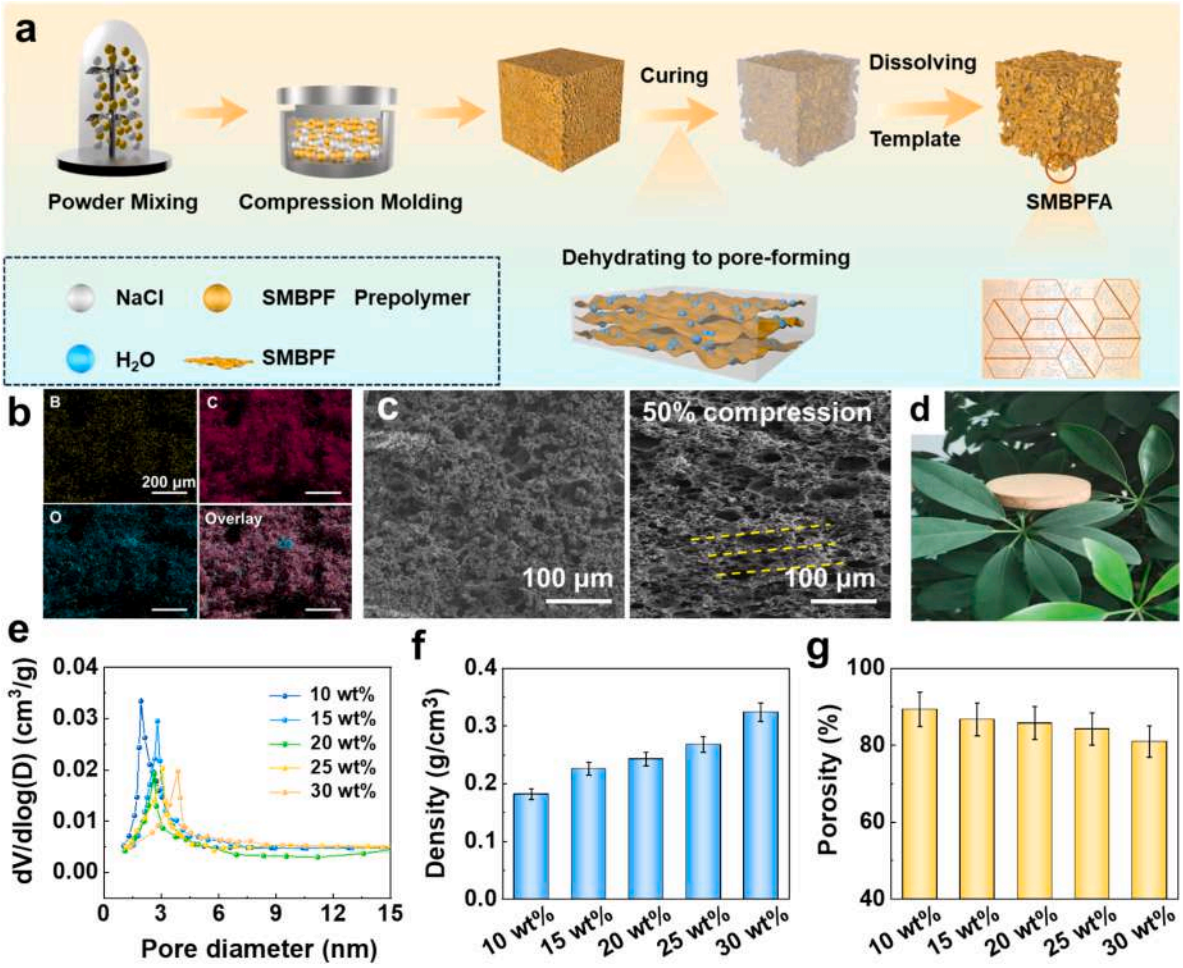

Fig. 4. Construction and properties of SMBPFAs. a) Schematic illustration for the preparation of SMBPFAs. b-c) The SEM images of SMBPFAs. d) The pictures of SMBPFAs. e) The pore size distribution of SMBPFAs. f) The density of SMBPFAs. g) The porosity of SMBPFAs.

porous architecture bestowed on the aerogel had an exceptionally low density, ensuring its dimensional stability when applied to plant leaves, as depicted in Fig. 4d. The BET test was employed to investigate the nanopore size distribution in SMBPFAs, revealing a diverse range of pore sizes spanning from 3 to 6 nm. Furthermore, nitrogen adsorption/desorption isotherms showed that the SMBPFAs exhibited an impressively high specific surface area of approximately 85 m^2/g (Fig. 4e and Fig. S8). The augmentation of the SMBPF content in the aerogels, led to a corresponding increase in the aerogel density. Notably, the 10 %-SMBPFA specimen exhibited the lowest density at 0.18 g/cm^3, while the 30 %-SMBPFA specimen demonstrated the highest density at 0.32 g/cm^3. The low density contributed to the high porosity of the SMBPFAs, and the specimens with lower densities exhibited greater porosities. Specifically, 10 %-SMBPFA displayed an exceptional porosity of 89.2 %, whereas 30 %-SMBPFA exhibited a comparatively lower porosity of 80.9 %, as illustrated in Figs. 4f and 4 g.

3.5. Shape memory mechanism of SMBPFAs

SMBPFAs exhibit completely different mechanical properties at room temperature and high temperature, with the energy provided by high temperatures intensifying the motion of the chain segment room temperature and high temperature, with the energy provided by high temperatures intensifying the motion of the chain segments, thus causing SMBPFAs to demonstrate variable stiffness properties with temperature. The stress–strain curves of the SMBPFAs under compression are illustrated in Fig. 5a, showing a three-stage compression process at room temperature. Stage I corresponds to elastic deformation, characterized by a linear augmentation in stress with the magnitude of deformation, typically ranging from 3 % to 5 %. With a gradual increase in deformation, the compression process enters stage II, wherein the SMBPFAs undergo plastic deformation. The rate of strain increment decreased with increasing deformation, resulting in the bending and collapse of certain pore walls. Consequently, a stress plateau was formed, which was characterized by approximately 35 % deformation occurring within this stage. As the compression process advanced further, the SMBPFAs transitioned into a densification phase where the vesicles within them were completely fragmented and adjacent pore walls were compressed into contact with each other. This led to a sharp surge in stress under minimal deformation. The compression mode of DMA was employed to evaluate the dynamic mechanical properties of the SMBPFAs, and the DMA curve is shown in Fig. 5b. By identifying the temperature corresponding to the tan delta peak, the T_g of SMBPFAs was found to be 98 °C, which closely resembled that observed for SMBPF-3. The energy storage modulus gradually decreased with increasing temperature for the SMBPFAs, exhibiting a sharp decline to its minimum level near T_g followed by a plateau. At this temperature, the SMBPFAs could be assigned to temporary shapes.

The shape memory cycle curves of the SMBPFAs are shown in Fig. 5c and S9. The SMBPFAs were compressed to 30 % deformation at temperatures higher than T_g; after fixing the shape and cooling, they were able to complete the restitution process under the effect of heat. The shape memory mechanism of the SMBPFAs is illustrated in Fig. 5d. Upon surpassing T_g, the mobility of the molecular chain segments increased,

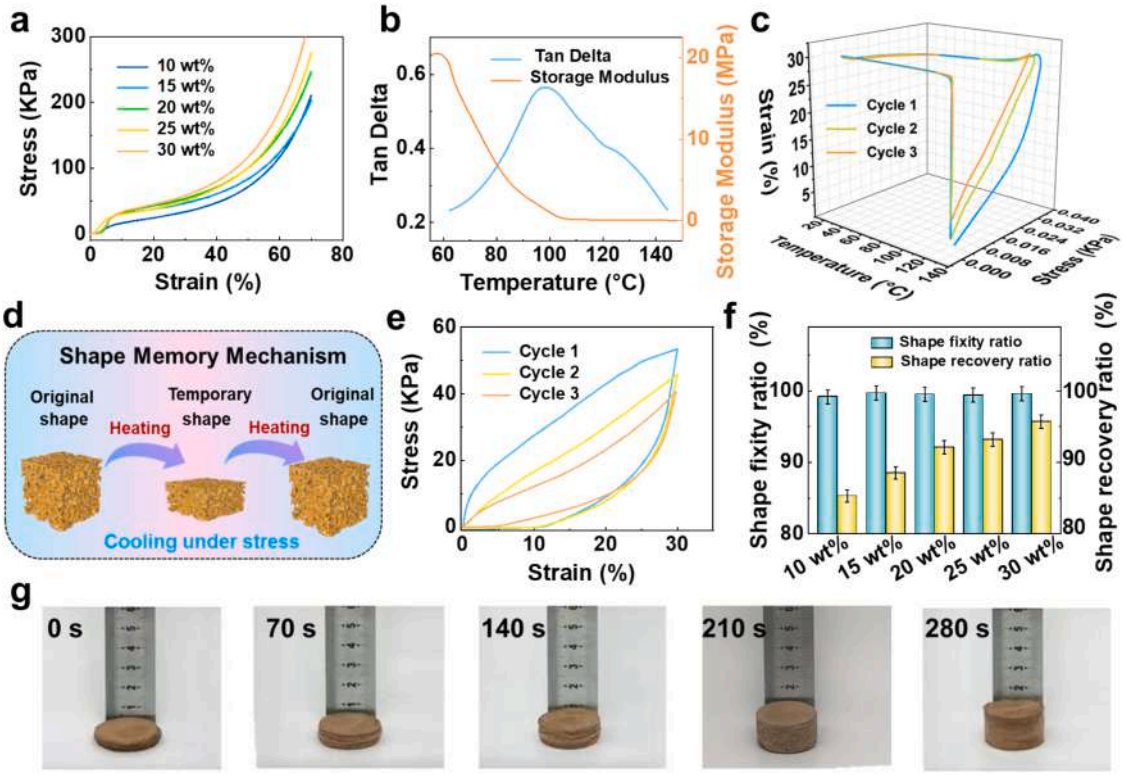

Fig. 5. Shape memory performance of SMBPFAs. a) The compressive stress–strain curves of SMBPFAs. b) The DMA curves of SMBPAs. c) The shape memory cycle curves of SMBPFAs. d) The shape memory mechanism of SMBPFAs. e) The compression cycle curves of SMBPFAs at high temperatures. f) The shape fixity ratio and shape recovery ratio of SMBPFAs. g) The shape recovery process of SMBPFA.

resulting in a decrease in the material stiffness. This facilitated the deformation of the SMBPFAs into temporary shapes under the applied pressure. The fixed shape of the material after cooling was achieved through the immobilization of the molecular chain segments until thermal stimulation was reapplied to the SMBPFAs, enabling the reconfiguration of the molecular chain segments and subsequent shape recovery. The shape memory performance of the SMBPFAs was exceptional for all three shape memory cycles. The SMBPFAs underwent high-temperature compression cycles at 120 °C above the T_g of the SMBPFAs. In contrast to compression at room temperature, the modulus of the SMBPFAs exhibited a significant reduction at elevated temperatures, facilitating effortless compression by 30 % of their original deformation and subsequent rebound upon load removal, as depicted in Fig. 5e. However, owing to the energy dissipation during each rebound, an increase in the number of compressions resulted in higher energy consumption by the SMBPFAs and posed challenges for the complete recovery of their initial shape. Consequently, this led to a decrease in the stress required for subsequent compression. The shape fixity and recovery rates of the SMBPFAs are elegantly depicted in Fig. 5f, with all SMBPFAs showing a remarkable shape fixity rate exceeding 98 %. Moreover, the shape recovery rate of the SMBPFAs exhibited a positive correlation with resin content. Remarkably, the highest observed shape recovery rate was attained with 30 wt%-SMBPFA containing an abundant resin content of 95.7 %. The SMBPFA took 280 s to recover from the temporarily compressed shape to its initial shape, and its recovery process in a heating oven is shown in Fig. 5g.

3.6. Thermal insulation performance of SMPBFAs

The exceptional thermal insulation performance of aerogels is derived from their ultrahigh porosity, which serves as a cornerstone for their application in thermal protection systems. Moreover, the generation of nanopores during the in-situ polymerization process further enhanced the thermal insulation capabilities of the SMPBFAs. The thermal insulation performance of 12 mm-SMBPFAs was evaluated on a heated platform at 200 °C by measuring the cold-side temperature using thermocouples (Fig. 6a and 6b). The SMBPFAs exhibited exceptional thermal insulation properties, with 10 wt%-SMBPFA demonstrating the highest level of insulation owing to its lowest apparent density. After a testing duration of 350 s, this sample achieved an impressively low cold-side temperature of only 43.8 °C. Under the influence of the thermal insulation performance of SMBPFAs, the temperature disparity between the cold-side and the hot-side of the sample exceeded 156 °C. Conversely, 30 wt%-SMBPFA displayed relatively inferior thermal insulation performance, resulting in a higher cold-side temperature of 48.9 °C. Compared to traditional thermal insulation materials (e.g., cotton), the SMBFAs exhibited better thermal insulation performance. As shown in Figs. S10 and S11, 30 wt%-SMBPFA had been subjected to heating on a 200℃-heating platform for 15 min and the temperature of its cold side had been 5℃ lower than that of cotton of the same thickness. SMBPFAs also showed good thermal insulation performance on the cooling platform, as shown in Figs. S12 and S13. On the cooling platform below 0℃, the hot surface temperature of the aerogel only decreased from 24℃ to 21℃ at room temperature after a long period of one-way cooling. This indicated that the aerogel had good thermal insulation performance, which endowed it with the prospect of application in the field of building thermal insulation. The thermal conductivity of a material plays a pivotal role in assessing its thermal insulation performance. In this investigation, the thermal conductivity of the SMPBFA specimens were determined both at room temperature and at 100 °C, as illustrated in Fig. 6c. Owing to the lower thermal conductivity of air within the aerogel vesicles compared to that of the pore walls, a negative relationship exists between the porosity and thermal conductivity of the SMPBFAs. Among all the tested samples, the sample with the highest porosity (10 wt%-SMPBFA) exhibited exceptional thermal insulation performance with a minimum thermal conductivity of 0.066 W/mK.

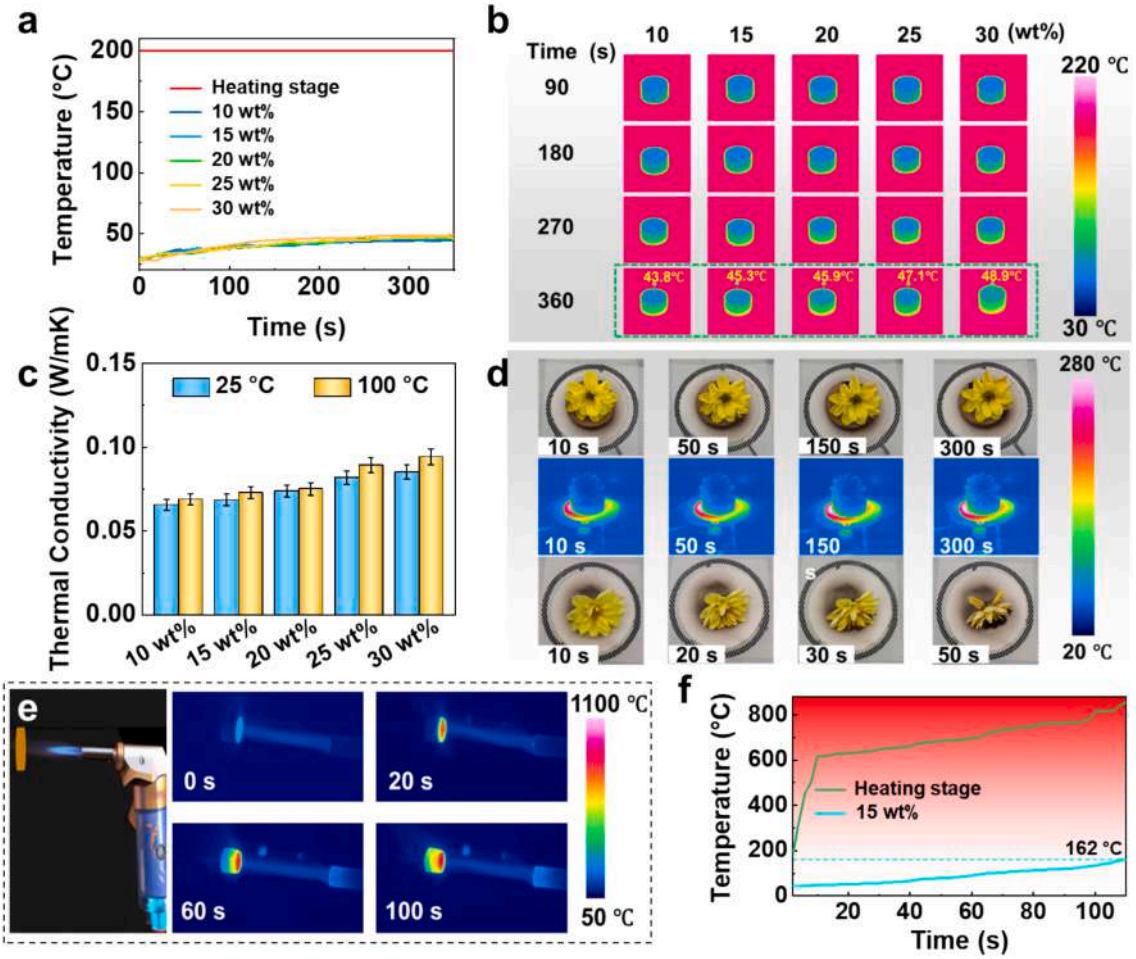

Fig. 6. Thermal insulation performance of SMBPFAs. a) The temperature records of SMBPFAs and the heating stage. b) The thermal imaging pictures of SMPBFAs thermal insulation performance test. c)The thermal conductivity of SMBPFAs measured by HOT-DISK. d) The infrared thermal imaging image of SMPBFAs and flowers. e-f) The demonstration of thermal protection performance of SMPBFAs under butane flame.

Furthermore, when comparing SMPBFAs at 100 °C with those at room temperature, the experimental results showed that an increase in temperature led to a slight increase in thermal conductivity of approximately 5 – 8 %.

As shown in Fig. 6d, a freshly picked flower was placed on an asbestos mesh and subsequently heated with an alcohol burner. Through continuous high-temperature baking, the flower gradually underwent noticeable shrinkage, commencing at the 20-second mark and culminating in complete charring by 40 s. In contrast, another freshly picked flower was positioned atop an aerogel before being placed on the asbestos mesh for baking. Surprisingly, even after enduring a full 40 s of heating, this flower remained unscathed, with only faint traces of baking injury under sustained high-temperature conditions that persisted for up to 200 s. This process was carefully observed using an infrared camera. Despite the localized temperature of the asbestos mesh reaching as high as 300 – 400 °C during the baking process, the temperature at the top of the aerogel consistently remained below 60 °C. Thus, the aerogel provided immense protection to the flower against potential dehydration due to the high temperatures. The thermal insulation capability of SMPBFAs can be attributed to three primary factors. First, the pore size of the SMPBFAs was smaller than the mean free path of air, which impeded thermal convection within the aerogel. Second, the micro-nano porous structure of SMPBFAs hindered continuous heat flow transfer in solids, restricting it to travel solely along the walls of the pores and creating an elongated pathway for thermal conductivity that effectively slowed down heat transfer. In addition, the predominantly closed pore structure of the SMPBFAs acted as a multitude of baffles, preventing heat flow transfer while forming multiple reflective interfaces that weakened heat conduction. In addition to their exceptional thermal insulation properties, the SMPBFAs also demonstrated effective ablative heat protection. As depicted in Fig. 6e–6f and Video S4, a 15-mm sample of SMPBFA exhibited remarkable resistance against direct exposure to a butane flame gun for a duration of 100 s. Despite the hot-side temperature reaching 800 °C, the cold-side temperature remained unwavering at 162 °C, thus highlighting its capability to function effectively in extremely high-temperature environments.

3.7. Potential applications of SMBPFAs

The shape memory properties of the SMPBFAs enabled them to exhibit controlled and regulated thermal insulation capabilities. After a 30 % compression deformation, the SMPBFAs were restored to various temporary shapes to evaluate their insulation performance on a heated platform at 100 °C. The thermal insulation performance of the SMPBFAs decreased when they were deformed to 30 % compression, as depicted in Fig. 7a and 7b, owing to a reduction in porosity. This resulted in a surface temperature of 44.2 °C after 400 s. The SMPBFAs were subjected to thermal stimulation in their temporary shape, resulting in recoveries of 20 %, 10 %, and 0 % deformation, respectively. The experimental results demonstrated that the temperature of the cold side of the SMPBFAs consistently decreased during shape recovery, owing to the progressive enlargement of aerogel pores and the subsequent increase in porosity, which significantly enhanced the thermal insulation performance. This phenomenon exemplifies the remarkable capability of

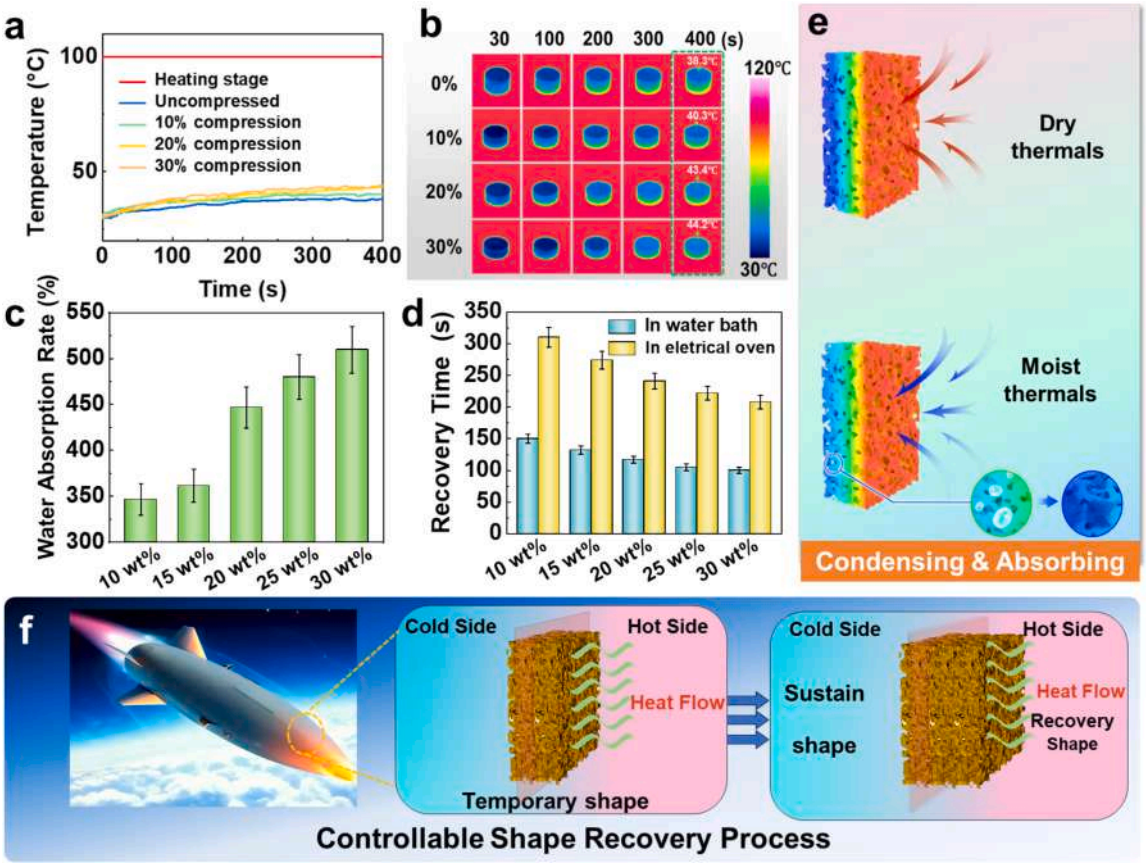

Fig. 7. The potential applications of SMBPFA. a-b) The temperature records and thermal imaging pictures of SMBPFAs when recovered to different levels of deformation in the shape recovery process. c) The water absorption of SMBPFAs. d) The recovery speed of SMBPFA in hot water and oven. e) The heat conduction mechanism of SMPBFAs in different media. f) The controllable shape recovery process of SMPBFAs.

shape memory polymer-based functional materials to achieve precise regulation of thermal insulation performance through shape recovery, thereby effectively meeting the diverse requirements of various application scenarios. The hydrophilic properties of SMPBFAs can be attributed to their molecular structures, which include abundant hydroxyl groups that facilitate the formation of hydrogen bonds with water. Moreover, the exceptional water absorption capability of SMPBFAs was enabled by their unique porous structures. Fig. 7c illustrates the results of the water absorption rate test for SMPBFAs, showing that the 30 wt %-SMPBFAs demonstrated a remarkable absorption rate of up to 500 %. Consequently, immersion in hot water led to a more rapid recovery of the SMPBFAs than heating in an oven (Fig. 7d). Specifically, the specimens exposed to hot water exhibited approximately twice as fast reversion as those subjected to conventional heating. Fig. S14 and Video S5 show the controllable shape memory restitution process of the SMPBFA. Half of the compressed SMPBFA was immersed in scalding water, whereas the other half was exposed to ambient air. The SMPBFA parts submerged in scalding water exhibited complete shape restitution within 120 s, whereas the parts exposed to air retained their shape without undergoing any restorative changes. This observation can be ascribed to the disparate thermal conduction mechanisms of the aerogels in different media. The thermal conduction mechanisms of the aerogels in different media are shown in Fig. 7e. When dry-hot gas flowed through the aerogel, heat was transferred to its porous structure at a low rate owing to the low thermal conductivity of the gas. Conversely, when water vapor traversed the aerogel, it condensed into small droplets that adhered to the aerogel under reduced-temperature conditions. These droplets were subsequently absorbed by the aerogel, facilitating the transition from gas-to-liquid heat transfer. This change in the thermal conductivity mechanism enhanced the overall thermal conductivity of the aerogel and consequently accelerated the recovery speed for the SMPBFAs.

The SMBPFAs, integrating shape memory and heat insulation capabilities, possess intelligent thermal insulation properties. SMBPFAs are capable of spontaneously reverting to their original shape upon heat sensing. During this process, both the microscopic pores and the macroscopic thickness of the aerogel expand, enhancing its thermal insulation performance and thereby realizing the smart thermal insulation functionality. Moreover, the controllable shape memory properties and the on-demand tuning of the thermal insulation properties provide the basis for the use of SMPBFAs in smart thermal protection systems. The outer surface of a flight vehicle is expected to be subjected to scorching temperatures during flight, whereas the interior would be maintained at a comparatively cool temperature, as illustrated in Fig. 7f. When the external SMPBFAs were exposed to heightened temperatures, atmospheric water vapor adhered to or infiltrated the aerogel surface and pores. By actively sensing both elevated temperatures and moisture content, the SMPBFAs dynamically regained their original shape, thereby effectively regulating the thermal insulation performance and ensuring a consistently low temperature on the inner side of the material. The aforementioned explanation underscores the intriguing potential of the application of SMPBFAs for temperature regulation within a flight vehicle by adjusting their porosity during the shape memory process. The internal temperature of the flight vehicle can be kept relatively stable by varying their thickness via controlling the shape recovery process of the SMPBFAs. Consequently, SMPBFAs with regulated thermal insulation properties exhibit significant promise for applications in smart thermal protection systems.

4. Conclusion

In summary, SMBPFs with tunable glass transition temperatures ranging from 75 to 189 °C and good high-temperature resistance were designed and synthesized for the first time via a hyperbranched topology design strategy. The mechanical properties of the PFs were improved, and they were endowed with shape memory properties without sacrificing their thermal stability. Benefitting from the boron-oxygen bonding and abundant benzene rings, the SMBPFs exhibited good ablation properties, with a line ablation rate of 0.043 mm/s and a mass ablation rate of 0.080 g/s, both of which are the best levels reported for shape memory resins. Based on this, SMBPFAs with an ultra-low density of 0.18 g/cm^3 and high porosity of 89.3 % were prepared from NaCl as a template using the in-situ polymerization strategy. The SMBPFAs exhibited excellent thermal insulation properties at both low (200 °C) and high (800 °C) temperatures. Moreover, the preparation method of the aerogels had no negative impact on the shape memory properties of the SMBPFs, which exhibited ultrahigh shape fixing ability and restitution rates. The synergistic effect of shape memory and thermal insulation performance enabled the SMBPFAs to provide tunable thermal insulation on demand, whereas the thermal insulation performance of the aerogels in temporary shapes could be improved by the shape recovery process. This pioneering discovery provides new ideas for smart thermal protection systems and new options for the design of thermal protection materials, that are expected to broaden the application areas of shape memory aerogels.

CRediT authorship contribution statement

Likai Hu: Writing – original draft, Methodology, Investigation, Data curation. **Lan Luo:** Writing – review & editing, Formal analysis. **Fenghua Zhang:** Resources, Funding acquisition. **Yanju Liu:** Writing – review & editing, Validation, Funding acquisition, Formal analysis. **Jinsong Leng:** Writing – review & editing, Resources, Funding acquisition.

Declaration of competing interest

The authors declare that they have no known competing financial interests or personal relationships that could have appeared to influence the work reported in this paper.

Acknowledgements

We thank the National Natural Science Foundation of China (Grant No. 92271112 and No. 92271206) for the support of this work.

Appendix A. Supplementary data

Supplementary data to this article can be found online at https://doi.org/10.1016/j.cej.2025.159558.

Data availability

Data will be made available on request.

References

[1] C. Liu, M. Wang, J. Wang, G. Xu, S. Zhang, F. Ding, Double-Phase-Networking Polyimide Hybrid Aerogel with Exceptional Dimensional Stability for Superior Thermal Protection System, Small 20 (44) (2024), https://doi.org/10.1002/smll.202404104.

[2] S. Zhang, J. Wang, Z. Wang, G. Xu, Y. Jiang, Y. Xiao, F. Ding, Reusable Nanoporous Al_2O_3-Containing Polyimide Aerogels for Thermal Insulation of Aircraft, ACS Appl. Nano Mater. 6 (17) (2023) 15925–15936, https://doi.org/10.1021/acsanm.3c02863.

[3] S. Zhang, Z. Wang, H. Ji, J. Wang, K. Lu, G. Xu, Y. Xiao, F. Ding, Mechanically Robust Nanoporous Polyimide/Silica Aerogels for Thermal Superinsulation of Aircraft, ACS Appl. Nano Mater. 6 (9) (2023) 7269–7279, https://doi.org/10.1021/acsanm.3c00384.

[4] X.Y. Chang, X.T. Cheng, H. Zhang, W.J. Li, L.J. He, X. Yin, X.Y. Liu, J.Y. Yu, Y. T. Liu, B. Ding, Superelastic Carbon Aerogels: An Emerging Material for Advanced Thermal Protection in Extreme Environments, Adv. Funct. Mater. 33 (26) (2023), https://doi.org/10.1002/adfm.202215168.

[5] X.C. Lin, S.L. Li, W.X. Li, Z.H. Wang, J.Y. Zhang, B.W. Liu, T. Fu, H.B. Zhao, Y. Z. Wang, Thermo-Responsive Self-Ceramifiable Robust Aerogel with Exceptional Strengthening and Thermal Insulating Performance at Ultrahigh Temperatures, Adv. Funct. Mater. 33 (27) (2023), https://doi.org/10.1002/adfm.202214913.

[6] O. Uyanna, H. Najafi, Thermal protection systems for space vehicles: A review on technology development, current challenges and future prospects, Acta Astronaut. 176 (2020) 341–356, https://doi.org/10.1016/j.actaastro.2020.06.047.

[7] P.Z. Gu, L.L. Lu, X. Yang, Z.Y. Hu, X.Y. Zhang, Z.J. Sun, X. Liang, M.X. Liu, Q. Sun, J. Huang, G.Q. Zu, Highly Stretchable Semiconducting Aerogel Films for High-Performance Flexible Electronics, Adv. Funct. Mater. (2024), https://doi.org/10.1002/adfm.202400589.

[8] Y. Li, X.F. Liu, X.Y. Nie, W.W. Yang, Y.D. Wang, R.H. Yu, J.L. Shui, Multifunctional Organic-Inorganic Hybrid Aerogel for Self-Cleaning, Heat-Insulating, and Highly Efficient Microwave Absorbing Material, Adv. Funct. Mater. 29 (10) (2019), https://doi.org/10.1002/adfm.201807624.

[9] E. Cuce, P.M. Cuce, C.J. Wood, S.B. Riffat, Toward aerogel based thermal superinsulation in buildings: A comprehensive review, Renew. Sustain. Energy Rev. 34 (2014) 273–299, https://doi.org/10.1016/j.rser.2014.03.017.

[10] R.W. Pekala, ORGANIC AEROGELS FROM THE POLYCONDENSATION OF RESORCINOL WITH FORMALDEHYDE, J. Mater. Sci. 24 (9) (1989) 3221–3227, https://doi.org/10.1007/bf01139044.

[11] K. Hirano, M. Asami, Phenolic resins-100 years of progress and their future, React. Funct. Polym. 73 (2) (2013) 256–269, https://doi.org/10.1016/j.reactfunctpolym.2012.07.003.

[12] C.F. Yuan, D.G. Wang, Y.J. Zhang, K. Li, J. Ding, Research progress on preparation, modification, and application of phenolic aerogel, Nanotechnol. Rev. 12 (1) (2023), https://doi.org/10.1515/ntrev-2023-0109.

[13] Y. Shiraishi, T. Hagi, M. Matsumoto, S. Tanaka, S. Ichikawa, T. Hirai, Solar-to-hydrogen peroxide energy conversion on resorcinol-formaldehyde resin photocatalysts prepared by acid-catalysed polycondensation, Communications Chemistry 3 (1) (2020), https://doi.org/10.1038/s42004-020-00421-x.

[14] X. Wei, X.H. Li, K.X. Wang, J.S. Chen, Design of Functional Carbon Composite Materials for Energy Conversion and Storage, Chem. Res. Chin. Univ. 38 (3) (2022) 677–687, https://doi.org/10.1007/s40242-022-2030-0.

[15] C. Wu, H. Huang, X.Y. Jin, X.J. Yan, H.B. Wang, Y.W. Pan, X.H. Zhang, C.Q. Hong, Water-assisted synthesis of phenolic aerogel with superior compression and thermal insulation performance enabled by thick-united nano-structure, Chem. Eng. J. 464 (2023), https://doi.org/10.1016/j.cej.2023.142805.

[16] X.F. Jia, W.D. Song, W. Chen, C. Ma, J.T. Wang, W.M. Qiao, L.C. Ling, Facile fabrication of lightweight mullite fiber/phenolic ablator with low thermal conductivity via ambient pressure impregnation, Ceram. Int. 47 (19) (2021) 28032–28036, https://doi.org/10.1016/j.ceramint.2021.06.136.

[17] Z.L. Yu, Y.C. Gao, B. Qin, Z.Y. Ma, S.H. Yu, Revitalizing Traditional Phenolic Resin toward a Versatile Platform for Advanced Materials, Acc. Mater. Res. 5 (2) (2024) 146–159, https://doi.org/10.1021/accountsmr.3c00194.

[18] H. He, L.Y. Geng, F. Liu, B. Ma, W.X. Huang, L.J. Qu, B.S. Xu, Facile preparation of a phenolic aerogel with excellent flexibility for thermal insulation, Eur. Polym. J. 163 (2022), https://doi.org/10.1016/j.eurpolymj.2021.110905.

[19] H. Huang, C.Q. Hong, X.Y. Jin, C. Wu, W. Wang, H.B. Wang, Y.W. Pan, S.Q. Wu, X. J. Yan, W.B. Han, X.H. Zhang, Facile fabrication of superflexible and thermal insulating phenolic aerogels backboned by silicone networks, Composites Part a-Applied Science and Manufacturing 164 (2023), https://doi.org/10.1016/j.compositesa.2022.107270.

[20] Y.Y. Sun, C.H. Chen, Interpenetrating Polymer Network of Blocked Polyurethane and Phenolic Resin. I. Synthesis, Morphology, and Mechanical Properties, Polymer Engineering and Science 51(2) (2011) 285-293. doi: 10.1002/pen.21826.

[21] X.Q. Liu, Y. Li, X.L. Xing, G.J. Zhang, X.L. Jing, Fully recyclable and high performance phenolic resin based on dynamic urethane bonds and its application in self-repairable composites, Polymer 229 (2021), https://doi.org/10.1016/j.polymer.2021.124022.

[22] S. Lin-Gibson, Cresol novolac /epoxy networks: Synthesis, properties, And Processability (2001).

[23] J.X. Li, C. Ren, D. An, Y.J. Ren, K.S. Moon, C.P. Wong, Systematic evaluation of cyanate ester/epoxidized cresol novolac copolymer resin system for high temperature power electronic packaging applications, Polymer 195 (2020), https://doi.org/10.1016/j.polymer.2020.122454.

[24] Y.D. Deng, F.H. Zhang, Y.J. Liu, J.S. Leng, Design and Synthesis of Shape Memory Phenol-Formaldehyde with Good Irradiation Resistance, Thermal, and Mechanical Properties, Acs Applied Polymer Materials 4 (8) (2022) 5789–5799, https://doi.org/10.1021/acsapm.2c00719.

[25] L.K. Hu, F.H. Zhang, L. Luo, L.L. Wang, Y.J. Liu, J.S. Leng, Design and preparation of shape memory phenol-formaldehyde foam composites with excellent thermal stability and mechanical properties, Composites Part a-Applied Science and Manufacturing 174 (2023), https://doi.org/10.1016/j.compositesa.2023.107738.

[26] M. Aghvami-Panah, A. Wang, M. Panahi-Sarmad, S.A.S. Esfahani, A.A. Seraji, M. Shahbazi, R. Ghaffarian, S. Jamalpour, X. Xiao, A comparison study on polymeric nanocomposite foams with various carbon nanoparticles: adjusting radiation time and effect on electrical behavior and microcellular structure, International Journal of Smart and Nano Materials 13 (3) (2022) 504–528, https://doi.org/10.1080/19475411.2022.2107110.

[27] L.-H. Ma, S.-D. Wang, J. Liu, H. Gao, W. Zhou, The design and investigation of hydrogel-based metamaterials with ultra large negative hygroscopic expansion ratio, International Journal of Smart and Nano Materials 13 (1) (2022) 114–129, https://doi.org/10.1080/19475411.2022.2049393.
[28] Z.C. Lou, R. Li, P. Wang, Y. Zhang, B. Chen, C.X. Huang, C.C. Wang, H. Han, Y.J. Li, Phenolic foam-derived magnetic carbon foams (MCFs) with tunable electromagnetic wave absorption behavior, Chem. Eng. J. 391 (2020), https://doi.org/10.1016/j.cej.2019.123571.
[29] S. Valkama, A. Nykänen, H. Kosonen, R. Ramani, F. Tuomisto, P. Engelhardt, G. ten Brinke, O. Ikkala, J. Ruokolainen, Adv. Funct. Mater. 17 (2) (2007) 183–190, https://doi.org/10.1002/adfm.200600604.
[30] Q. Yue, J.L. Li, Y. Zhang, X.W. Cheng, X. Chen, P.P. Pan, J.C. Su, A.A. Elzatahry, A. Alghamdi, Y.H. Deng, D.Y. Zhao, Plasmolysis-Inspired Nanoengineering of Functional Yolk-Shell Microspheres with Magnetic Core and Mesoporous Silica Shell, J. Am. Chem. Soc. 139 (43) (2017) 15486–15493, https://doi.org/10.1021/jacs.7b09055.
[31] Q. Quan, C.L. Fan, N.A. Pan, M.H. Zhu, T. Zhang, Z. Wang, Y. Dong, Y.K. Wu, M. Tang, X.Y. Zhou, M.Z. Chen, Tough and Stretchable Phenolic-Reinforced Double Network Deep Eutectic Solvent gels for Multifunctional Sensors with Environmental Adaptability, Adv. Funct. Mater. 33 (36) (2023), https://doi.org/10.1002/adfm.202303381.
[32] Q.Q. Lan, C. Feng, Z.C. Wang, L. Li, Y. Wang, T.X. Liu, Chemically Laminating Graphene Oxide Nanosheets with Phenolic Nanomeshes for Robust Membranes with Fast Desalination, Nano Lett. 21 (19) (2021) 8236–8243, https://doi.org/10.1021/acs.nanolett.1c02683.
[33] R.Y. Sha, X.P. Cheng, J.X. Dai, Y.F. Zu, Y.Y. Zeng, J.J. Sha, Lightweight phenolic resin aerogel with excellent thermal insulation and mechanical properties via an ultralow shrinkage process, Mater. Lett. 324 (2022), https://doi.org/10.1016/j.matlet.2022.132626.
[34] Z.L. Yu, Z.Y. Wu, S. Xin, C. Qiao, Z.Y. Yu, H.P. Cong, S.H. Yu, General and Straightforward Synthetic Route to Phenolic Resin Gels Templated by Chitosan Networks, Chem. Mat. 26 (24) (2014) 6915–6918, https://doi.org/10.1021/cm504036u.
[35] X.C. Liu, J.C. Sun, F. Yuan, C.S. Ye, R.B. Zhang, Lightweight, flexible, and heat-insulated phenolic impregnated carbon ablator (PICA) with adjustable flexibility and high compressive resilience property, J. Appl. Polym. Sci. 139 (9) (2022), https://doi.org/10.1002/app.51712.
[36] Y. Yang, Y.M. Yang, L. Ye, T. Zhao, H. Li, Microphase separation regulation of polyurethane modified phenolic resin aerogel to enhance mechanical properties and thermal insulation, Chem. Eng. J. 495 (2024), https://doi.org/10.1016/j.cej.2024.153532.
[37] Z.L. Yu, G.C. Li, N. Fechler, N. Yang, Z.Y. Ma, X. Wang, M. Antonietti, S.H. Yu, Polymerization under Hypersaline Conditions: A Robust Route to Phenolic Polymer-Derived Carbon Aerogels, Angewandte Chemie-International Edition 55 (47) (2016) 14623–14627, https://doi.org/10.1002/anie.201605510.
[38] Z.L. Yu, N. Yang, V. Apostolopoulou-Kalkavoura, B. Qin, Z.Y. Ma, W.Y. Xing, C. Qiao, L. Bergström, M. Antonietti, S.H. Yu, Fire-Retardant and Thermally Insulating Phenolic-Silica Aerogels, Angewandte Chemie-International Edition 57 (17) (2018) 4538–4542, https://doi.org/10.1002/anie.201711717.
[39] V.T. Le, N. San Ha, N.S. Goo, Advanced sandwich structures for thermal protection systems in hypersonic vehicles: A review, Composites Part B-Engineering 226 (2021), https://doi.org/10.1016/j.compositesb.2021.109301.
[40] X.L. Xing, Y.H. Zhao, X.T. Zhang, J. Wang, T. Hong, Y. Li, S.J. Wang, C.S. Zhang, X. L. Jing, Healable ablative composites from synergistically crosslinked phenolic resin, Chem. Eng. J. 447 (2022), https://doi.org/10.1016/j.cej.2022.137571.
[41] R.X. Hu, F.H. Zhang, L. Luo, L.L. Wang, Y.J. Liu, J.S. Leng, An end-capping strategy for shape memory phthalonitrile resins via annealing enables conductivity and wave-absorption, Chem. Eng. J. 489 (2024), https://doi.org/10.1016/j.cej.2024.150956.
[42] L. Luo, Z.H. Niu, R.X. Hu, F.H. Zhang, Y.J. Liu, J.S. Leng, Triple-shape memory polybenzoxazine resins and their composites, Composites Part a-Applied Science and Manufacturing 177 (2024), https://doi.org/10.1016/j.compositesa.2023.107910.
[43] X.F. Wang, Y. He, X.L. Xiao, Y.J. Liu, J.S. Leng, Properties of shape memory polyimide composites with continuous “brick-and-mortar” layered structure: High flame retardancy, ablation resistance, and high mechanical properties, Composites Part a-Applied Science and Manufacturing 181 (2024), https://doi.org/10.1016/j.compositesa.2024.108151.